Available online at www.sciencedirect.com
SCIENCE DIRECT
Journal of Catalysis 229 (2005) 82–96
JOURNAL OF CATALYSIS
www.elsevier.com/locate/jcat

Synthesis of carbon nanofibers: effects of Ni crystal size during methane decomposition

De Chen [a,*], Kjersti O. Christensen [a], Ester Ochoa-Fernández [a], Zhixin Yu [a], Bård Tøtdal [b], Nieves Latorre [c], Antonio Monzón [c], Anders Holmen [a]

[a] *Department of Chemical Engineering, Norwegian University of Science and Technology (NTNU), N-7491 Trondheim, Norway*
[b] *Department of Physics, NTNU, N-7491 Trondheim, Norway*
[c] *Department of Chemical and Environmental Engineering, University of Zaragoza, E50009 Zaragoza, Spain*

Received 27 July 2004; revised 14 October 2004; accepted 15 October 2004

Available online 24 November 2004

Abstract

The effect of the crystal size of Ni on the growth of carbon nanofibers (CNFs) was studied in a tapered oscillating element microbalance reactor. Small Ni crystals yield a low growth rate and fast deactivation and thus a low final yield of CNF. Large Ni crystals reduce the growth rate because of low surface area. An optimum growth rate and yield of carbon nanofibers can be achieved on optimally sized Ni crystals (around 34 nm). A model has been proposed for interpreting the kinetic effects of the Ni crystal size based on a detailed mechanism of the carbon nanofiber growth. The reduced coking rate on a small-sized Ni crystal is a result of increased saturation concentration of CNF and thus a low driving force for carbon diffusion through the Ni crystals. As a consequence, the surface coverage of carbon increases, which enhances the formation of encapsulating carbon and thus the deactivation. Both the low initial coking rate and the fast deactivation result in a low yield of carbon nanofibers on small-sized crystals. The results also indicate that hydrogen has a significant effect on the formation of CNF, and an optimum partial pressure of hydrogen exists for the CNF growth.

Keywords: Nickel catalyst; Crystal size; Carbon nanofibers; Growth mechanism TEOM; Methane decomposition

1. Introduction

Carbon nanotubes (CNTs) and carbon nanofibers (CNFs) have many unique properties, such as high resistance to strong acids and bases, high electric conductivity, high surface area, and high mechanical strength [1,2]. These unique properties result in many potential applications, such as catalyst supports [3], selective adsorption/absorption agents [4], hydrogen storage [5], composite materials [6], nano-electronic and nano-mechanical devices [7], and field emission devices [8]. The term "carbon nanotube" is normally used to refer to a structure with the basal carbon planes parallel to the tube axis. "Carbon nanofiber" is a more general term referring to graphite structures with other orientations of the graphene plane, and CNTs can be considered a special case of CNFs. Therefore, CNFs are used in the present work.

Chemical vapor deposition (CVD) has long been extensively used for the production of CNF [9–12], in which Ni, Co, and Fe and their alloys have proved to be efficient catalysts. Carbon sources are not very restricted, and many hydrocarbons, such as C_1–C_6, have been studied [2,13]. Among these, the catalytic decomposition of methane on Ni catalysts is one the most extensively studied systems [2,14–17]. The main driving force for such studies is the abundance and cheapness of natural gas, as well as the importance of filamentous carbon formation in steam methane reforming [17,18]. Methane decomposition on Ni has long been studied to obtain detailed kinetic and mechanistic information about carbon formation, with the intention of avoid-

* Corresponding author. Fax: +47 73595047.
E-mail address: chen@chembio.ntnu.no (D. Chen).

0021-9517/$ – see front matter
doi:10.1016/j.jcat.2004.10.017

ing carbon formation in steam reforming of natural gas [17–20]. On the other hand, methane decomposition was found to be en efficient way to produce CNF/CNT [2].

Catalyst plays a key role in the production of CNFs. Much research work has been devoted to the development of efficient catalysts for large-scale production of CNFs. The effect of preparation methods, supports, and texture promoters of Ni catalysts has been studied by Ermakova et al. [14,21]. They noticed that the yield of carbon produced by methane decomposition is possibly related to the average size of the nickel particles on the fresh catalysts, and that the maximum yield is observed at a particle size of 20–60 nm [21]. The strong effect of the Ni crystal size on carbon formation is possibly not surprising, since it was reported almost 30 years ago that the thermodynamic equilibrium constant or the coking threshold during methane decomposition can be directly related to the crystal size of Ni [18]. It was proposed that this can be related to the changes in thermodynamic properties of carbon nanofibers due to the external tension energy of carbon nanofibers as a function of the crystal size.

Much work has been devoted to size-controlled synthesis of CNFs [22–26]. It is generally observed that a metal particle is at the tip of a CNF during reaction, and that the diameter of the CNF is approximately identical to the diameter of the metal particle. It is therefore logical to assume that it is possible to control the diameter of CNFs by controlling the size of the catalyst metal particle. Direct evidence for this strategy has recently been provided by Cheung et al. [25], who found that the diameters of carbon nanofibers produced by ethene decomposition at 1073 K were almost identical to the diameter of the Fe particles.

However, the fact that the metal particle size at the tip of a CNF is identical to the diameter of the CNF does not mean that the diameter of CNFs is always controlled by the metal particle size, since the metal particles might undergo reconstruction, sintering, and fragmentation. De Jong et al. [2] have made a review of the synthesis of CNFs from methane decomposition and from synthesis gas. It was found that the diameter of CNFs changed with the operating conditions and the composition of the reactant mixture. To add even more complexity, an in situ XRD study [27] showed that Ni particles underwent serious reconstruction and that the Ni crystal size reaches a constant value, regardless of initial size. Therefore, a detailed understanding of the effect of the metal crystal size on the formation of CNFs is still highly desirable. More importantly, based on our knowledge, only very little attention has been paid to the possible kinetic effects of metal crystal size on CNF growth [28].

The present work deals with the preparation and characterization of Ni catalysts with different crystal sizes. The study has been designed to gain an understanding of the effect of the Ni crystal size on the rates of CNF growth and deactivation, and thus on the yield of CNF (g_{CNF}/g_{cat}). The relationship between metal crystal size and the diameter of CNFs is studied by TEM. A mechanism of CNF growth is proposed for better understanding of the effect of Ni crystal size.

2. Experimental

2.1. Materials

Hydrotalcite materials with different Mg/Al ratios were supplied by Condea (Pural). The hydrotalcite supports are named as HT 30, 50, and 70, where the numbers represent the weight percentage of MgO. Ni (11 wt%) supported on $CaAl_2O_4$ is an industrial reforming catalyst. α-Al_2O_3 was supplied by Alcoa Chemicals.

2.2. Catalyst preparation

A series of Ni catalysts was prepared by incipient wetness impregnation on the different supports. The composition and properties of the catalysts are listed in Table 1. The hydrotalcite precursors were dried for 24 h at 383 K before impregnation. The support materials were impregnated with a calculated quantity of an aqueous solution of $Ni(NO_3)_2 \cdot 6H_2O$. The catalysts were dried overnight at 383 K. The oxide-supported Ni catalysts were calcined in air at 873 K for 4 h and reduced in 50 mol% H_2/Ar (total flow of 100 ml/min) at 873 K.

To completely isolate the effects of Ni crystal size on CNF growth, a comparison of CNF formation on crystals

Table 1
Catalyst composition and BET surface area (S_{BET}), specific surface are of Ni (S_{Ni}) and NiO crystal size (Dp^1) determined from XRD and Ni crystal size Dp^2 determined by chemisorption

Catalyst	Ni (%)	MgO (%)	CaO (%)	Al_2O_3 (%)	S_{BET} (m^2/g_{cat})	S_{Ni} (m^2/g_{cat})	Dp^1 (nm)	Dp^2 (nm)
Ni/HT30	12.5	24.5		59.6	271	8.6	12	12
Ni/HT50	12.5	42.6		41.5	201	4.2	24	23
Ni/HT70	12.5	59.5		24.6	228	4.2	29	24
Ni/HT50-24h	12.5	42.6		41.5	201		34	
Ni/HT50-50h	12.5	42.6		41.5			32	
Ni/HT50-74h	12.5	42.6		41.5			47	
Ni/$CaAl_2O_4$	11		8	81	5.5	0.33		220
Ni/α-Al_2O_3	11			89	0.6	0.037		1629

of different sizes has been made on a support of HT50. The different Ni crystal sizes on HT50 have been obtained by sintering of Ni catalysts for different periods (50 and 74 h) at a total pressure of 2 MPa in a mixture of $H_2O/H_2/Ar$ (1/0.23/0.85) prior to the methane decomposition. Another sintering experiment was performed under steam reforming conditions at a total pressure of 2 MPa in a mixture of $H_2O/CH_4/Ar$ (1/0.51/0.57) for 24 h. The sintering was performed separately in a fixed bed reactor.

2.3. Catalyst characterization

Temperature-programmed reduction (TPR) was performed in a quartz reactor heated by an electrical furnace at a heating rate of 10 K/min in a mixture containing 7 mol% H_2, at a maximum temperature of 1203 K. Hydrogen consumption was measured by analyzing the effluent by means of a thermal conductivity detector. The steam formed during the reduction was removed by a cooling trap.

The BET surface area of the supports was measured by N_2 adsorption at 77 K in a Coulter^{TM} SA 3100. The specific surface area of Ni was measured in a Micromeretics ASAP 2010 C V2.01. Volumetric hydrogen chemisorption was measured at 305 K, and the samples were heated and reduced before hydrogen adsorption. The volume adsorbed was obtained by making two subsequent isotherms, with evacuation to 10^{-5} Torr for 30 min in between. The difference between the two isotherms was used to calculate the surface area and the dispersion of Ni, assuming an adsorption stoichiometry of $H/Ni = 1$. Approximately 1 g of sample was used for analysis.

X-ray powder diffraction (XRD) analysis of the samples was performed with a Siemens D5000 X-ray diffractometer. Phase identifications were carried out by comparing the collected spectra with spectra in the database. The average size of the metal particle was calculated with the Scherrer equation based on peak broadening.

The Ni catalysts have also been examined with a scanning transmission electron microscope (STEM), a JEOL 2000EXII electron microscope equipped with a field emission gun capable of giving a lattice resolution of 0.14 nm. Both bright-field and annular dark-field images were obtained to get a better contrast of Ni particles against support materials.

2.4. Synthesis of CNF in a TEOM

Synthesis of CNF was carried out in a tapered oscillating element microbalance (TEOM) reactor (Supplied by R&P, USA). The TEOM reactor can be operated up to 973 K and 50 bar. A glass element in TEOM oscillates at the natural frequency, and the frequency changes with the change of the mass of the sample in the sample carrier. The TEOM reactor measures the mass change in the reactor by measuring changes in frequency of the sample carrier [17,29]. The reactant mixture is forced to flow through the sample, which makes TEOM an excellent tool for kinetic studies including deactivation. However, special care taken because of the possible pressure drop in the reactor, since the volume of the sample will increase markedly as a result of CNF formation. The sample carrier volume used in the present work is about 100 cm^3. A relatively small amount of catalyst (typically 2–10 mg) is installed in the sample carrier. Two layers of quartz wool are placed on the top and the bottom of the sample carrier, and a relatively large void volume maintained in the catalyst bed for CNF formation. With this configuration, CNF mass can reach up to a few hundred grams per gram of catalyst without a significant pressure drop.

The catalyst was reduced in a 50 mol% H_2/Ar mixture, while the temperature was raised from ambient to 853 K at a rate of 2 °C/min, and the temperature was maintained at 853 K for 8 h. Preliminary isothermal kinetic reduction experiments showed that all of the catalyst is completely reduced under these conditions. The catalyst was then flushed in Ar for 10 min. Synthesis of CNF was carried out at 853 K and at atmospheric pressure. Hydrogen (5 ml/min) and 50 ml/min of a mixture of methane and nitrogen (90 mol% of methane) were fed to the reactor by means of mass flow controllers. In most cases, CNF synthesis was performed under steady-state conditions, and operating conditions were kept constant.

The effect of hydrogen partial pressure has been studied in experiments in which the evolution of carbon accumulation was monitored while the H_2 concentration was increased stepwise. This type of experiment allows us to investigate the influence of gas composition in a more rapid manner [30,31]. The flow rate of methane was kept constant at 100 ml/min and diluted with Ar. Experiments were carried out at 853 K and 30 kPa methane partial pressure. The hydrogen partial pressure was adjusted by replacement of Ar by hydrogen at constant total pressure.

The accumulation of CNF and the coking rates were recorded each minute. For the fast formation of CNF, the data can be recorded at time intervals as short as 0.86 s. The final yield of CNF is defined as the accumulated CNF per gram of catalyst at 30 min on stream during the steady-state experiments, where the catalyst has lost most of its activity.

2.5. Temperature-programmed synthesis of CNF

The temperature-programmed experiments were performed with the intention of studying nucleation and temperature dependence of CNF formation. These experiments were carried out with a conventional thermobalance (CI Electronics Ltd., U.K., model MK2) equipped with mass flow and temperature controllers. Catalyst reduction was carried out in situ at 700 °C for 2.5 h with the use of a H_2 (50%)/N_2 mixture. The reaction conditions were as follows: sample weight: 100 mg; temperature: from 550 to 650 °C; total flow rate: 675 Nml/min; feed composition ($\%CH_4/\%H_2/\%N_2$): from 2.5/0/97.5 to 10/5/85. During the

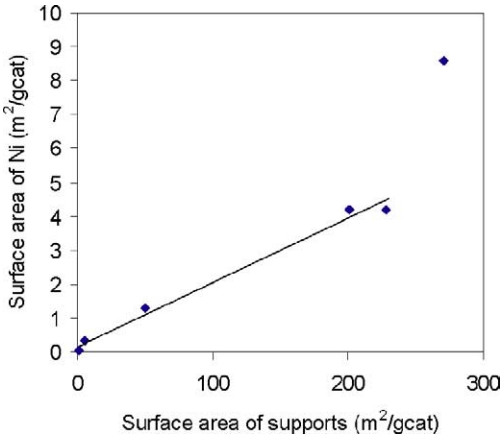

Fig. 1. Relationship between the surface area of Ni particles and the surface area of supports.

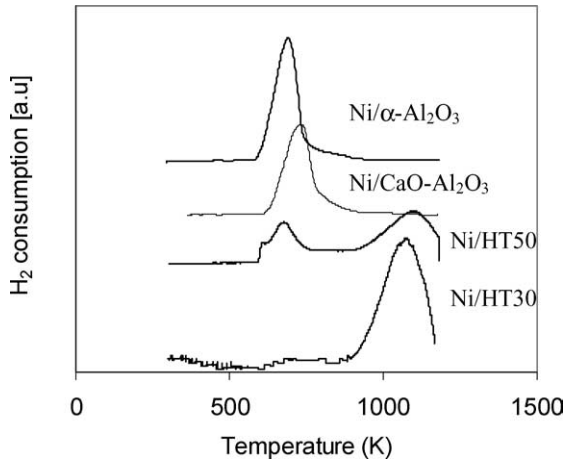

Fig. 2. Temperature-programmed reduction spectra of different Ni catalysts.

reaction, the temperature was increased at a rate of 10 K/min from 673 to 973 K and then kept at 973 K for 1 h.

2.6. Characterization of CNFs

The morphology and the diameter of CNFs were studied by high-resolution transmission electron microscopy (TEM) (JEOL 2000EXII). TEM specimens were prepared by ultrasonic dispersion of the slightly ground CNT samples in ethanol, and then a drop of the suspension was applied to a holey carbon copper grid. The samples were used as prepared without any subsequent purification.

3. Results

3.1. Characterization of the catalysts

The BET surface area of the supports, the specific surface area of the Ni particles, and the estimated Ni particle size based on chemisorption and XRD are presented in Table 1. The surface area of the supports varies over a large range, from 0.6 to 270 m^2/g_{cat}, resulting in large differences in the surface area of Ni and in the average crystal size. The relationship between the surface area of the supports and the Ni particles is presented in Fig. 1. The surface area of Ni is proportional to the surface area of the supports, except for the Ni on HT30, which has a surface area much larger than the others.

The specific surface area of Ni is generally higher on the hydrotalcite materials, since they have large surface areas due to the layered structures. The crystal size of Ni was calculated based on the dispersion (D) of the Ni particles:

$$Dp\ (\text{nm}) \approx \frac{1.01}{D}. \quad (1)$$

The Ni crystal size determined from chemisorption is almost identical to the NiO crystal size measured by XRD for most of the catalysts. It should also be pointed out that the XRD measurements of several reduced catalysts indicated that the reduced Ni crystals are only slightly smaller than the NiO crystals. Therefore, Ni or NiO crystal size is not clearly distinguished in the discussion.

The impregnated Ni catalysts exhibit very different reduction behavior, as shown in Fig. 2. The maximum temperature of the large peak in the TPR spectra increases with increasing surface area of the supports. The values are 425, 457, 580, and 1087 K for Ni on α-Al_2O_3, $CaAl_2O_4$, HT70, and HT30, respectively. Two reduction peaks were observed in the TPR spectra of Ni/HT70 and of NiO/HT30. For Ni/HT70 a large low-temperature peak was observed at 580 K and a small peak at 1180 K. For Ni/HT30 the small peak was located at 740 K and the large peak at about 1080 K.

After calcination at 873 K, the hydrotalcite materials lose their layered structure and become mixed metallic oxides. The XRD analysis in Fig. 3 shows mainly NiO on the hydrotalcite-derived supports. The mixed-metal oxide was not detected on HT50 and HT70, whereas it was detected on HT30, for which double peaks are observed (Fig. 3). Several Ni catalysts have been examined by STEM, and one example shown in Fig. 4 is the sample of Ni HT50. The results clearly indicate that good contrast is obtained by annular dark-field image, which excludes the central spot, collecting the single from all diffracted beams outside of a given solid angle. The visible spots in Fig. 4A and Fig. 5 were confirmed to be Ni particles by EDS maps, as shown in Fig. 4 on the right-hand side. Mg and Al seem to distribute uniformly. A distribution of the Ni crystal size has been clearly illustrated in Fig. 4, but most of the particles are rather small, as shown in Fig. 5 in detail. A statistical analysis of the crystal size distribution is shown in Fig. 6; the average Ni crystal size is 22 nm, which is almost identical to the value measured by XRD and chemisorption. Much worse contrast was found with Ni/HT30, which might be due to small crystal size. Again, detailed examination indicates that the average Ni crystal size is 12 nm for Ni/HT30, again identical to the value reported in Table 1.

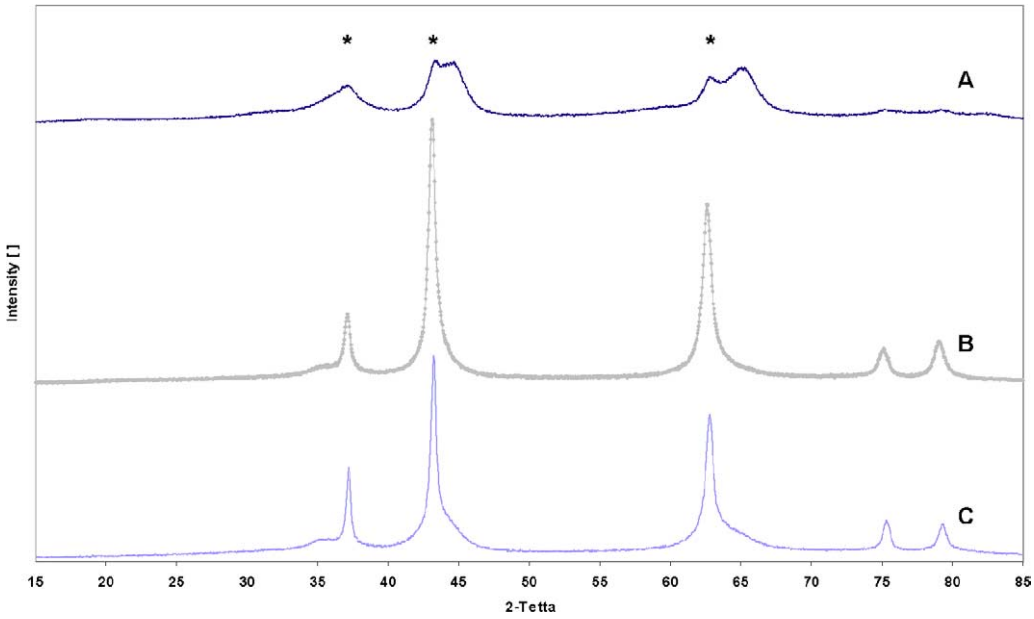

Fig. 3. XRD spectra of NiO (*) on different hydrotalcite derived supports. A: HT30, B: HT50, and C: HT70.

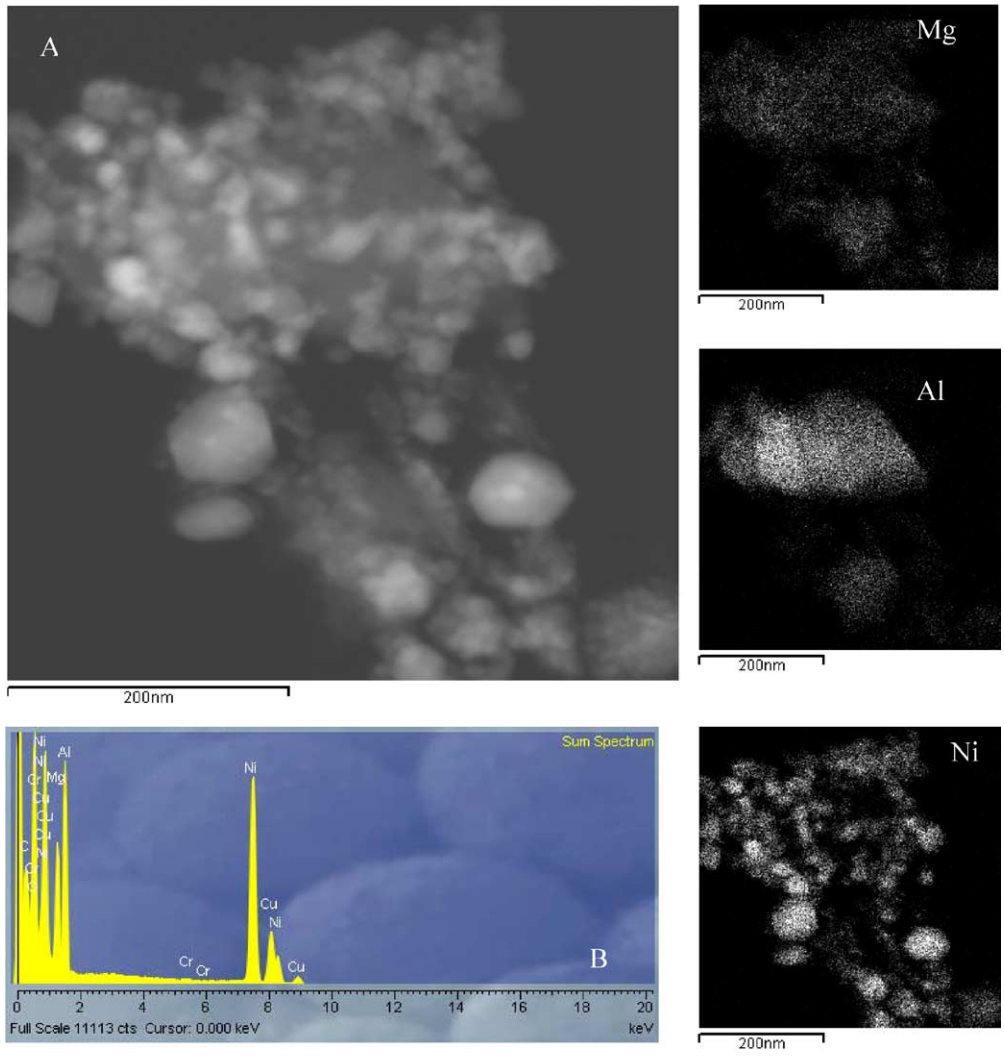

Fig. 4. EDS images of Ni/HT50. A: STEM, dark field image, B: EDX analysis, Right side: EDS maps of Mg, Al and Ni.

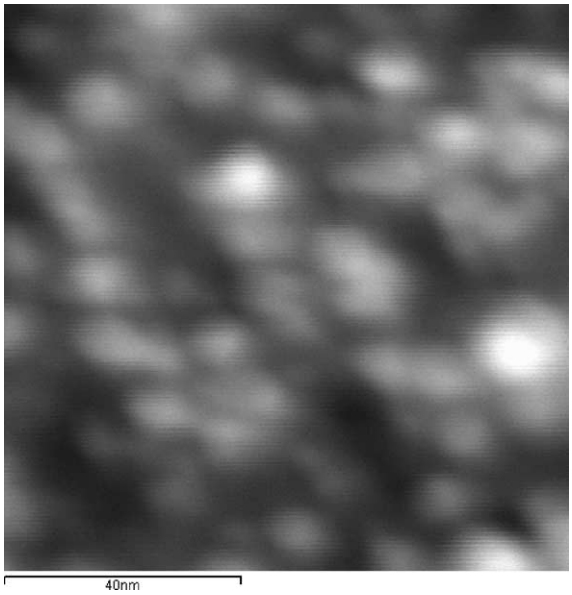

Fig. 5. STEM dark field images of Ni/HT50.

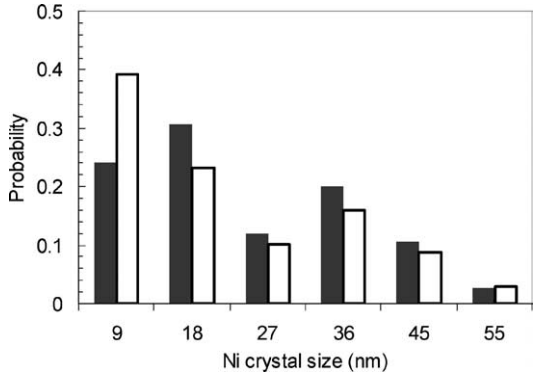

Fig. 6. Distribution of Ni crystal size and CNF diameter on Ni/HT50 measured by TEM. With color fill: Ni crystal size, without color fill: CNF diameter.

3.2. Synthesis of CNF at 853 K

The accumulation of CNF with time on stream on Ni crystals of different sizes supported on different supports is shown in Fig. 7A, and the corresponding growth rates are shown in Fig. 7B. The carbon formation can be divided into two different zones. Initially the coking rate is rather high, but the deactivation rate is also high, and the CNF synthesis reaches a relative steady-state growth in the second zone. The time scale for the first zone depends very much on the catalysts used, and this can possibly be related to effects of the Ni crystal size, which will be discussed later. To eliminate possible effects of the support, the dependence of CNF growth on Ni crystals has been studied further on Ni crystals of different sizes on an identical support (HT50), which were obtained by sintering for different times in the presence of steam in a fixed bed reactor. The results in both Figs. 7and 8,

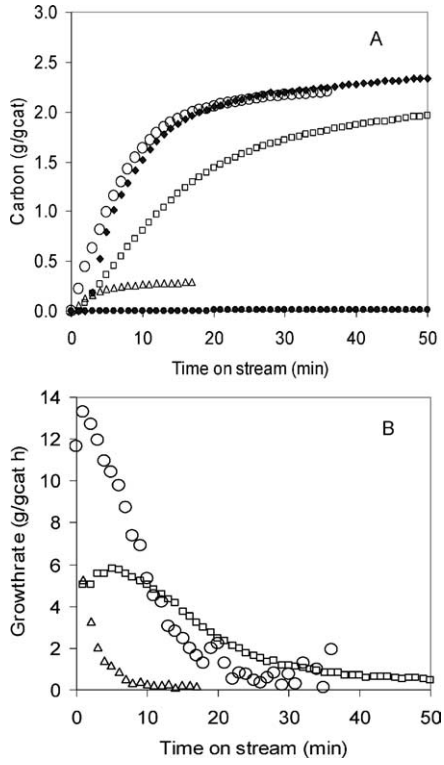

Fig. 7. Accumulation of CNF (A) and the rate of the accumulation (B) with time on stream on Ni/α-Al_2O_3 (●), Ni/CaO–Al_2O_3 (□), Ni/HT70 (○), Ni/HT30 (△) and Ni/HT50 (◆). Reaction conditions: $T = 853$ K, $P_{tot} = 100$ kPa, $P_{CH_4} = 80$ kPa, $P_{H_2} = 5.5$ kPa. Total flow: 50 ml/min.

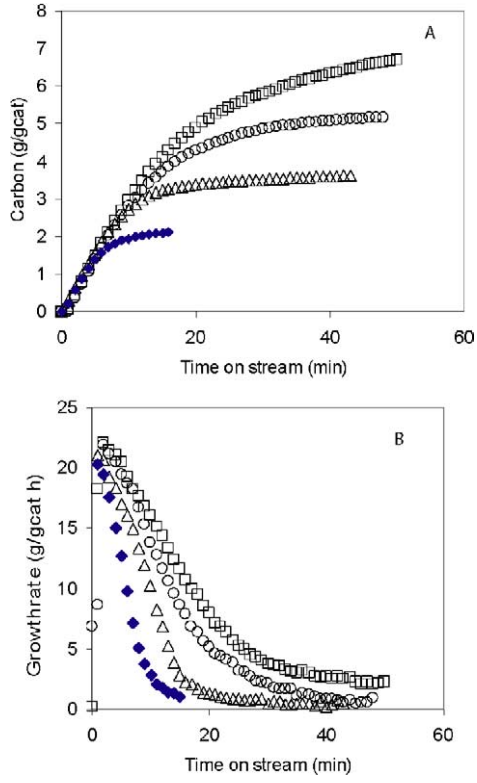

Fig. 8. Accumulation of CNF (A) and the rate of the accumulation (B) with time on stream on Ni/HT50 sintered (h): 0 (◆), 24 (□), 50 (○) and 74 (△). Reaction conditions are same as presented in Fig. 7.

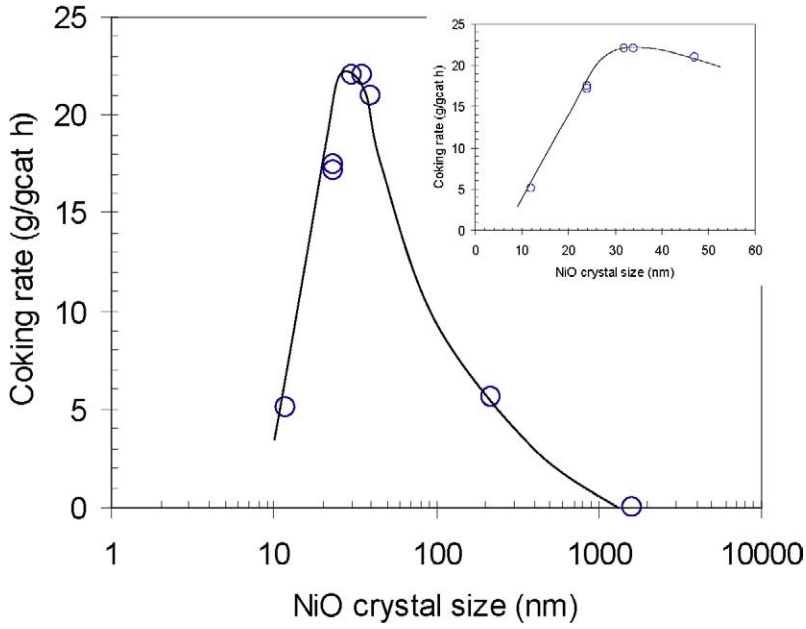

Fig. 9. Effects of NiO crystal size on the growth rate of CNF. Reaction conditions are same as presented in Fig. 7.

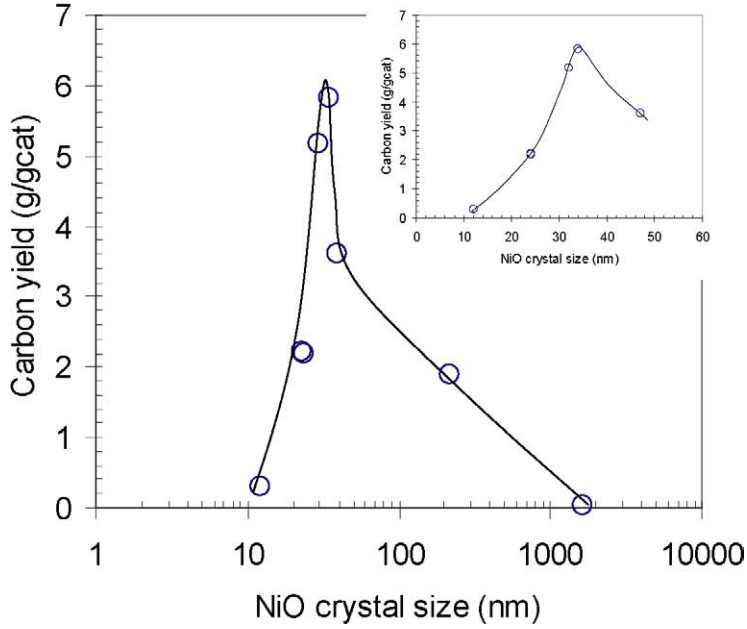

Fig. 10. Effects of NiO crystal size on the final carbon yield of CNF. Reaction conditions are same as presented in Fig. 7.

especially the latter, clearly reveal a very significant effect of Ni crystal size on CNF growth. The increase in theNi crystal size seems to influence initial growth rates only a little, but significantly affects deactivation rates. The rate of CNF growth follows the order Ni/HT50-24h > Ni/HT50-50h > Ni/HT50-74h > Ni/HT50(-0h), as shown in Fig. 8.

The initial CNF growth rates and the yields of CNF are plotted as a function of the Ni crystal size in Figs. 9 and 10, respectively, where Ni crystals on different supports are also included. The inserted figures are the magnification of relatively small crystals. The yields of CNF were taken at a time on stream of 30 min. Ni crystals that were too large or too small yielded low growth rates and low yield of CNF. Thedeactivation was found to be faster on smaller Ni crystals. This therefore clearly indicates an optimum Ni (NiO) crystal size of around 34 nm for CNF growth at the conditions used in the present work. Figs. 7 and 10 reveal that the CNF yield is extremely sensitive to the Ni crystal size, especially in the range of 20–40 nm. A small change in the Ni crystal size results in a considerable change in the CNF yield. In addition, it is interesting to note that CNF growth is almost identical on Ni/HT50 and Ni/HT70 with similar crystal size, regardless of the composition of the catalyst supports.

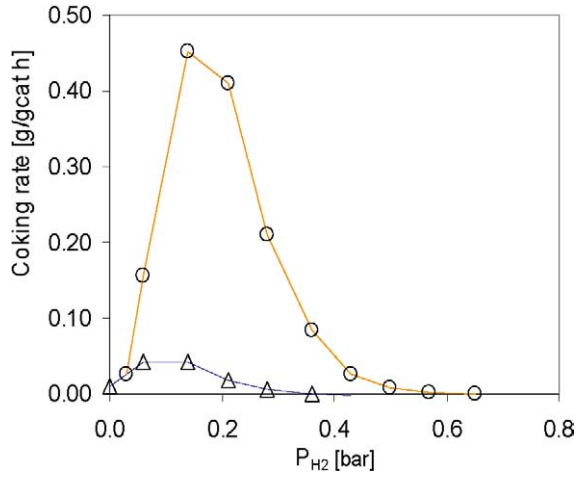

Fig. 11. Effect of partial pressure of methane on the accumulation rate of CNF on Ni/HT70 (○), Ni/HT30 (△). Reaction conditions: $T = 853$ K, $P_{tot} = 100$ kPa, $P_{CH_4} = 30$ kPa, total flow: 50 ml/min.

3.3. Effect of hydrogen on synthesis of CNF on two Ni crystals of different sizes

The CNF growth rates on catalysts with Ni crystal sizes of 12 and 24 nm at 853 K and different hydrogen partial pressures are illustrated in Fig. 11. The results indicate that both the partial pressure of hydrogen and the crystal size of Ni have very significant effects on the coking rates. In good agreement with the results presented above, the coking rate is lower on the smaller Ni crystals. Increasing the Ni crystal size from 12 to 24 nm yielded a difference in the coking rate of almost 10 times. However, the results in Fig. 11 clearly show an optimum in the partial pressure of hydrogen for the coking rate. The position of the optimal partial pressure of hydrogen seems to be slightly dependent on the Ni crystal size; however, the magnitude of this maximum rate is clearly affected by the size of the Ni particles.

3.4. Temperature-programmed synthesis of CNF

Fig. 12A shows the accumulation of CNF as a function of time on stream for Ni/HT30 and Ni/CaO–Al_2O_3 during temperature programming from ambient to 700 °C. In addition, the changes in CNF growth rates with temperature are presented in Fig. 12B. The two catalysts show a similar behavior. Carbon formation starts at a certain temperature ($T_{nucleation}$) for each catalyst. Then the CNF growth rate increases gradually with increasing temperature, until a maximum rate (r_{Cmax}) is reached at a given temperature (T_{max}). After the maximum, CNF growth rate decreases until a residual rate is reached, as a consequence of catalyst deactivation. Fig. 12 clearly indicates that the values of r_{Cmax}, T_{max}, and $T_{nucleation}$ depend significantly on the crystal size, and higher T_{max} and $T_{nucleation}$ were observed for the formation of CNF on smaller crystals (Ni/HT30) than on larger crystals (Ni/CaO–Al_2O_3). $T_{nucleation}$ is 697 and 761 K, T_{max} is 907 and 927 K for Ni/CaO–Al_2O_3 and Ni/HT 30, respectively. Consistent with the results presented above, the coking rate is higher for larger Ni crystals.

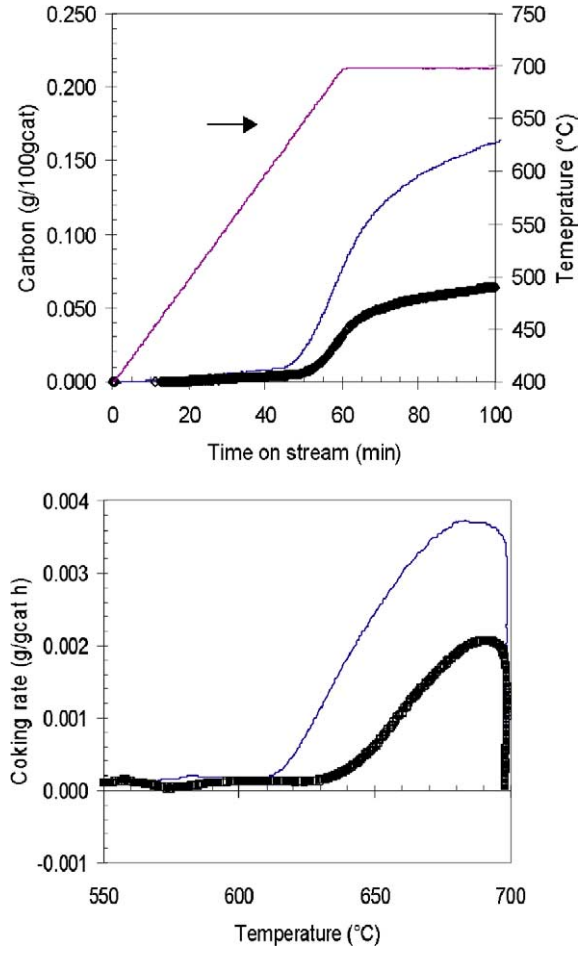

Fig. 12. Temperature-programmed synthesis: (A) accumulation of CNFs with time on stream and (B) rates of accumulation of CNFs on HT-30 (□), Ni/CaO–Al_2O_3 (line) at a methane partial pressure of 0.05 bar and a partial pressure of hydrogen of 0.1 bar.

3.5. Characterization of CNF by TEM

The diameter distribution and the morphology of the CNFs were studied by both high- and low-resolution TEM. Figs. 13 and 14 depict the CNFs produced on Ni/HT30 and Ni/HT50, respectively. The diameter distribution is also presented in the inserted figures in Figs. 13 and 14; this was measured by counting about 100 CNFs on the TEM images. It should be pointed out that the samples were as produced without purification. From the high-resolution images in Figs. 13B and 14B, it can be seen that the nanostructure is more or less identical for all of the CNFs, regardless of the catalyst used. It appears to be a typical fishbone structure, in which the graphene planes are orientated at an angle of about 45° with respect to the

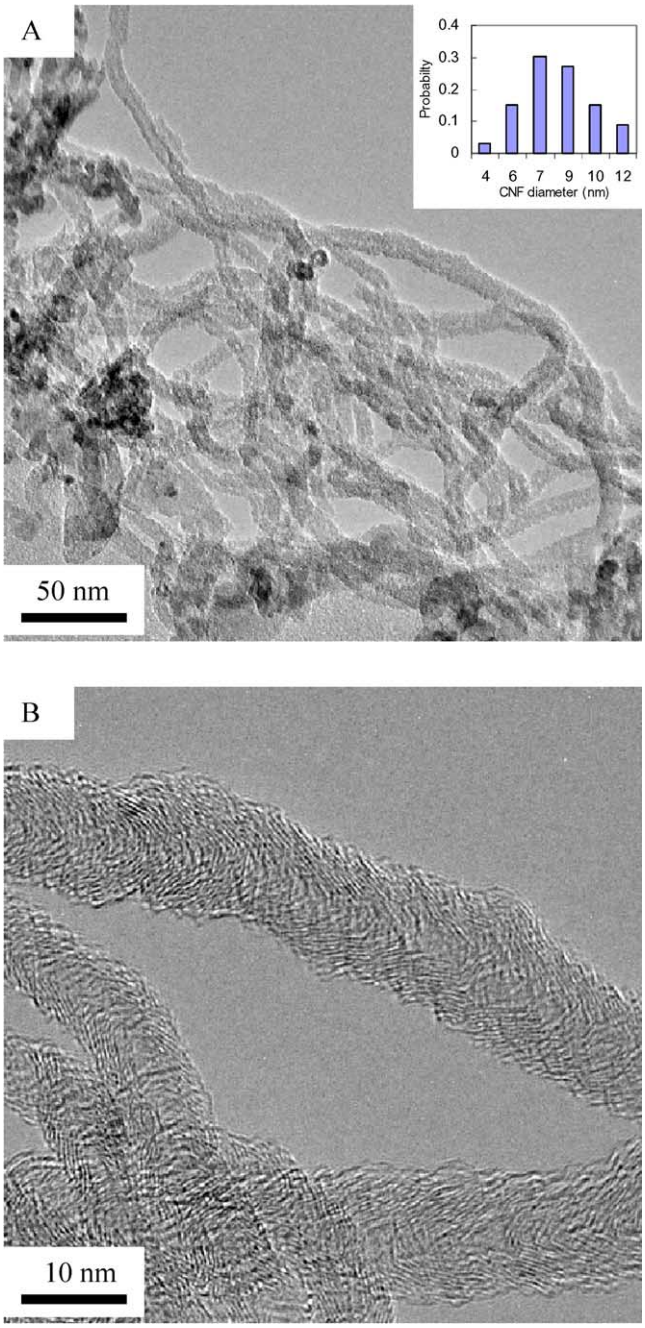

Fig. 13. TEM imagine of CNF produced on Ni/HT30 at 653 K.

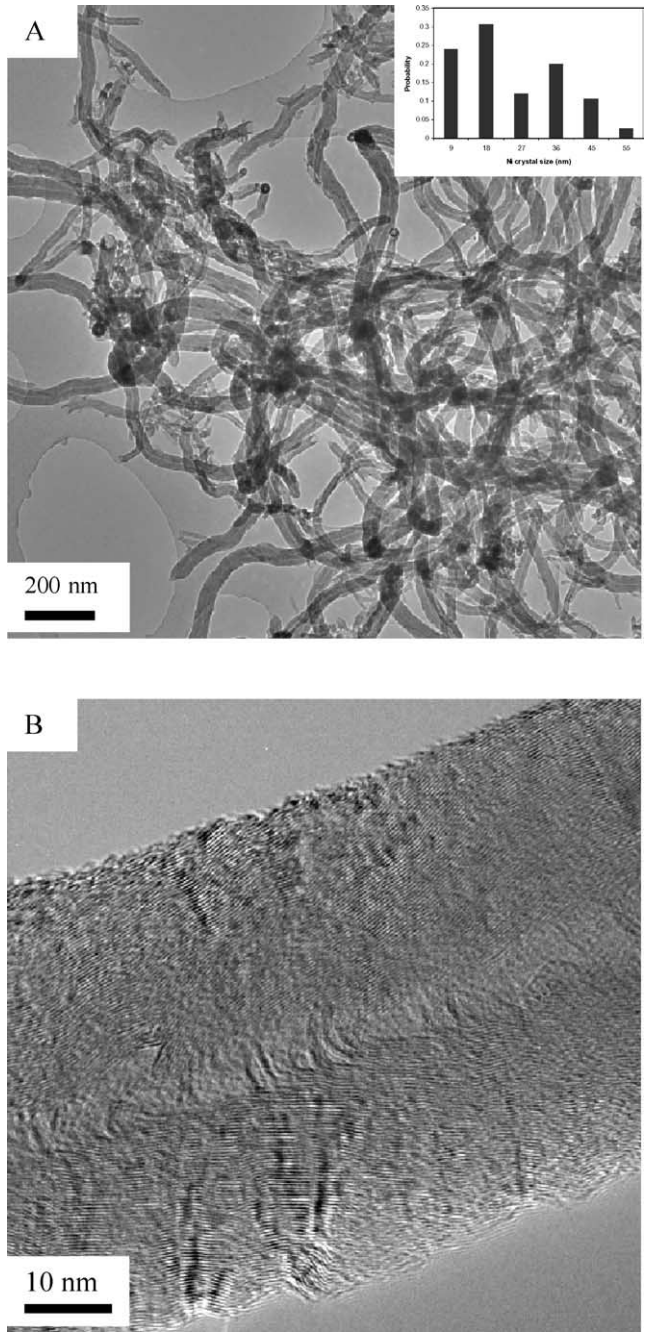

Fig. 14. TEM imagine of CNF produced on Ni/HT50 at 653 K.

axis of the fiber. The CNFs look rather pure from the TEM pictures, and no other forms of carbon were observed. These images also indicate a high crystallinity of the CNFs. However, it was found that the distribution of CNF diameters depends significantly on the catalyst. The distribution of CNF diameter produced on Ni supported on hydrotalcite-derived materials is relatively narrow, and the CNF diameters produced on Ni/HT30 are smaller than those produced on Ni/HT50. The average diameter of the CNFs is about 8 nm on Ni/HT30 and about 25 nm on Ni/HT50.

4. Discussion

4.1. Characterization of catalysts

As expected, the surface area of the supports plays a key role in determining the dispersion of Ni particles. Large surface area provides more surface sites for anchoring Ni precursors, resulting in better dispersion and thus a smaller crystal size. The lower surface area supports, such as α-Al_2O_3 and $CaAl_2O_4$ spinel, are typical supports for methane steam reforming at high temperatures and high

pressures in the presence of steam, because of their thermal stability. However, they seem not to be the preferred supports for CNF formation, as will be discussed in detail below.

In general, changes in the maximum reduction temperature reflect the extent of interaction between the catalyst precursor and the support. The observations that the maximum reduction temperature follows the order of the Ni crystal size and that the smaller the crystal size the higher the maximum temperature of reduction are in good agreement with the results in the literature [32–34].

Hydrotalcite-like materials have a composition of $[(M^{2+})_{(1-x)}(M^{3+})_x(OH)_2]^{x+}[(A^{n-})_{x/n} \cdot yH_2O]$, where M^{2+} and M^{3+} are metal ions with a valence of 2+ and 3+, respectively, and x is the ratio of $M^{2+}/(M^{2+} + M^{3+})$. The anion A^{n-} can be one of a number of anions such as carbonate. For pure hydrotalcite, M^{2+} is the Mg^{2+} and M^{3+} is the Al^{3+}. Hydrotalcite has a layered structure composed of molecular sheets. In each sheet, magnesium and aluminum ions are 6-fold coordinated in hydroxide, and the resulting octahedras share edges to form infinite sheets [35]. After calcination at relatively high temperatures, hydrotalcite decomposes into a metal oxide mixture. Results clearly indicate that the hydrotalcite-derived oxide mixtures are good supports, providing efficient anchoring sites for Ni nanoparticles. However, the Mg/Al ratio seems to have an effect on the dispersion of the Ni particles, and a low ratio (Mg/Al = 30) yields a better dispersion of Ni nanoparticles. Hydrotalcite-like materials have been recognized as promising catalyst precursors for different reactions [35,36]. The present work demonstrates that hydrotalcite materials with certain ratios of $Mg^{2+}/(Mg^{2+} + Al^{3+})$ are also promising supports for catalysts suitable for the production of CNFs.

XRD, STEM, and chemisorption of hydrogen have been used to measure the Ni crystal size, and as shown in Table 1 the values are almost identical for Ni crystals on different supports. The values obtained by STEM are consistent with the value measured by XRD and chemisorption. However, it has been shown that the measurement of crystal size by STEM depends very much of the location of the images; different distributions are demonstrated in Figs. 4 and 5. Although STEM can provide the crystal size distribution, XRD and chemisorption are much simpler techniques, and such values as reported in Table 1 are used in the present work to examine the effect of Ni crystal size on CNF formation. In any event, all of the results indicate that the Ni crystal size measured in the present work is reliable.

4.2. Effect of Ni crystal size on the synthesis of CNFs

All of the experiments in the present work, including the steady-state experiments (Figs. 7 and 8), sequential experiments (Fig. 11), and temperature-programmed experiments (Fig. 12), indicate a lower coking rate on the smaller Ni crystals and that there is an optimal crystal size for the synthesis of CNFs. The results in Fig. 12 also suggest that the initiation or nucleation of CNF is more difficult on the smaller Ni crystals. Our results strongly challenge the theory stated by Nazimek et al. [34]. They observed an increase in the coking rate and in the coking threshold (minimum steam to carbon ratio without carbon formation) with increasing mean crystal size of the Ni crystals during steam reforming of *n*-butane. They stated that the spillover of steam adsorbed to the surface of the support is the determining factor, where a higher coking rate and higher coking threshold on larger crystals is a result of lower concentration of steam on the Ni surface. Since there is more complicated dependence of the coking rate on the Ni crystal size during methane decomposition in the absence of steam, other factors must be important for determining such dependence.

The value for the coking threshold (minimum hydrogen-to-carbon ratio without carbon formation) during methane decomposition can be extrapolated from the curves in Fig. 11. The coking threshold is 1.3 on 12-nm Ni crystals, whereas it is about 2 on 24-nm Ni crystals. The fact that the coking threshold is higher on larger Ni crystals is in good agreement with previous observations [18]. Rostrup-Nielsen [18] has proposed an equation to take into account the effect of the crystal size on the Gibbs energy deviation from graphite (ΔG_C):

$$\Delta G_C = \frac{\gamma M}{\rho}\frac{1}{D} + \mu^* \tag{2}$$

where γ is the surface tension; M and ρ are the molecular weight and density, respectively; D is the diameter of the carbon filaments; and μ^* is the contribution from structure defects compared with graphite. The larger the crystal size, the closer the thermodynamic properties are to graphite, which yielded a high coking threshold.

However, the interpretation of the effect of crystal size on the coking rate is not straightforward, and no detailed explanation of the kinetic effects of the Ni crystal size has been presented so far. To understand CNF synthesis on crystals of different sizes, a mathematical model will be developed based on our experimental results and the published mechanism of the CNF growth.

The mechanism of formation of CNF that has generally been accepted includes hydrocarbon adsorption on the surface, conversion of the adsorbed hydrocarbon to adsorbed surface carbon via surface reactions, subsequent segregation of surface carbon into the layers near the surface, diffusion of carbon through Ni, and then precipitation on the rare side of the Ni particle [18,28,30,37]. The process will eventually lead to the formation of CNF, as presented in the following equations:

Surface reactions:

$$CH_4 + 2S = CH_3\text{–}S + H\text{–}S, \tag{3}$$

$$CH_3\text{–}S + S = CH_2\text{–}S + H\text{–}S, \tag{4}$$

$$CH_2\text{–}S + S = CH\text{–}S + H\text{–}S, \tag{5}$$

$$CH\text{–}S + S = C\text{–}S + H\text{–}S, \tag{6}$$

$$2H\text{–}S = H_2 + 2S. \tag{7}$$

Dissolution/segregation:

$$\mathrm{C\text{–}S} = \mathrm{C_{Ni.f}} + \mathrm{S}. \tag{8}$$

Diffusion of carbon through nickel:

$$\mathrm{C_{Ni.f}} \rightarrow \mathrm{C_{Ni,r}}. \tag{9}$$

Precipitation/dissolution of carbon:

$$\mathrm{C_{Ni.r}} = \mathrm{C_f}. \tag{10}$$

Encapsulating carbon formation:

$$n\mathrm{C\text{–}S} = \mathrm{C}_{\text{ encapsulating}}, \tag{11}$$

where S is the adsorption site; $C_{Ni,f}$ is the carbon dissolved in nickel at the front of the particle, just below the selvage; $C_{Ni,r}$ is the carbon dissolved in nickel at the rear of the particle (support side); $C_{encapsulating}$ represents the encapsulating carbon formation on the Ni surface, which deactivates catalysts; and n is the ensemble size for encapsulating carbon [38].

A microkinetic model has previously been developed that can deal with surface reactions of methane reforming on Ni surfaces in terms of elementary steps [38]. The model can be used to simulate the surface coverage under different conditions. However, deactivation has to be taken into account in a simulation of CNF formation. Therefore, no attempt has been made to simulate the kinetic data on crystals of different sizes in the present work, and only a qualitative analysis will be made. At steady state, the coking rate equals the rate of carbon diffusion through the Ni particles, which can be described as follows:

$$r = \frac{D_\mathrm{C}}{d_\mathrm{Ni}} a_\mathrm{Ni}(C_{\mathrm{C\_Ni.f}} - C_{\mathrm{C\_Ni,r}}), \tag{12}$$

where D_C is the effective diffusivity for carbon diffusion through the nickel particle, d_{Ni} is the effective length of carbon diffusion in the Ni particles, a_{Ni} is the specific surface area of Ni, $C_{C\_Ni,f}$ is the concentration of carbon in Ni at the gas side, and $C_{C\_Ni,r}$ is the carbon concentration at the rare side of Ni particles. The carbon formation is directly proportional to the driving force of diffusion. When the driving force reaches zero, the conditions are related to the coking threshold. Assuming that segregation of carbon is a fast process, $C_{C\_Ni,f}$ will be in equilibrium with surface carbon, which can be described by a Langmuir-type equation [39]:

$$\frac{\theta_\mathrm{C}}{1-\theta_\mathrm{C}} = \frac{x_\mathrm{b}}{1-x_\mathrm{b}} \exp\left(-\frac{\Delta G_\mathrm{seg}}{RT}\right),$$
$$\text{where } \Delta G_\mathrm{seg} = -4.52 \times 10^4 - 14.23T \text{ (J/mol)}, \tag{13}$$

where θ_C is the surface coverage of carbon and x_b is the weight fraction of carbon in the segregation layer of Ni (g_{carbon}/g_{Ni}). $C_{Ni,f}$ can be calculated from x_b. The precipitation of carbon from the dissolved phase has not yet been well studied. However, if it is assumed that precipitation is a fast step, the carbon in bulk Ni at the rare side is in equilibrium with CNFs. $C_{Ni,r}$ is therefore identical with the saturation concentration of CNFs (C_{sat}).

The Gibbs free energy of CNF depends on the nanostructure of CNF. The graphene sheet in the carbon nanofibers has a different orientation relative to the fiber axis. A cylindrical structure, namely multiwall carbon nanotube, is used as a probe in the present work, but the model based on CNT can easily be extended to CNF [40]. The tube has an outside diameter of $2r$ and a core diameter of $2r_i$, and a surface energy of γ_{bps} (reported in [40] to be 0.1 J/m^2). Tibbetts [41] has demonstrated how the radius of the cylindrical structure may be controlled by equilibrium thermodynamics. The surface tension energy of the basal plate of graphite is

$$\Delta G_\mathrm{s} = \gamma_\mathrm{bps} S = \frac{2\gamma_\mathrm{bps}}{\nu\pi(r-r_i)}. \tag{14}$$

Energy for bending of the basal plane is

$$\Delta G_\mathrm{Bend} = \frac{Ya^2 \ln(r/r_i)}{12\nu(r^2 - r_i^2)}, \tag{15}$$

where Y is Young's modulus, a is the interlayer spacing for graphite fiber, and ν is the concentration of graphite. The reported values [40] of 1×10^{12} J/m^3 for Young's modulus and 0.34 nm for the interlayer spacing were used in the present work.

Nolan et al. [40] pointed out that misalignment strain between graphite sheet layers in a nanotube should also be taken into account, since the typical stacking sequence in flat graphite would not be maintained in the nanotube configuration. The enthalpy for graphite stacking misalignment should be between the lower limit of 1000 J/mol (the variation of half the heat of sublimation per carbon atom of polycyclic aromatics) and an upper limit of 5300 J/mol (the enthalpy of turbostritic graphite). The misalignment entropy is estimated to be 3 J/(mol K), based on the half average entropy of melting per carbon atom of various small solid aromatic molecules. Nolan et al. [40] estimated an enthalpy of 1800 J/mol and an entropy of 3.6 J/(mol K) for graphite stacking misalignment based on fitting experimental data. These values are used in the present work without further modification.

The change in Gibbs free energy (ΔG_p) for precipitation of carbon in Ni bulk is then given by

$$\Delta G_\mathrm{p} = \Delta G_0 + \frac{2\gamma_\mathrm{bps}}{\nu\pi(r-r_i)} + \frac{Ya^2\ln(r/r_i)}{12\nu(r^2-r_i^2)} + \Delta G_\mathrm{mis}, \tag{16}$$

where ΔG_0 is the standard Gibbs energy change when a carbon atom precipitates from the dissolved phase, which can be considered a reverse process of segregation.

The thermodynamic equilibrium constant K for the precipitation can be calculated from

$$K = \frac{C_\mathrm{CNF}}{C_\mathrm{sat}} = \exp\left(-\frac{\Delta G_\mathrm{p}}{RT}\right), \tag{17}$$

where C_{CNF} is the concentration of CNF and C_{sat} is the saturation concentration of CNF in the Ni bulk phase. Fig. 15 illustrates the simulated equilibrium constant K as a function of the Ni crystal size, which is assumed to be identical

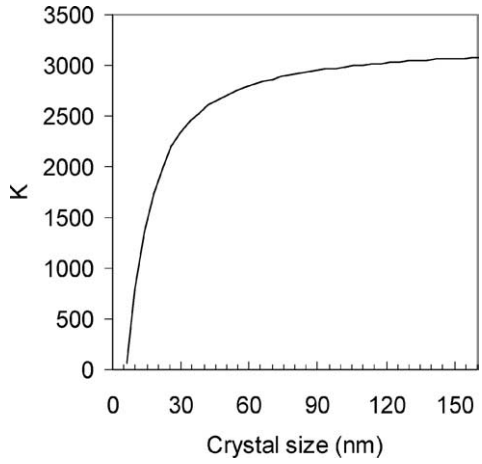

Fig. 15. Equilibrium constant K of carbon precipitation as function of crystal size. Core radius $r_i = 2$ nm.

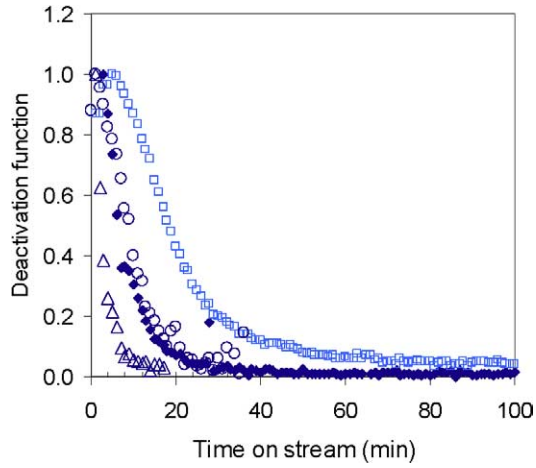

Fig. 16. Deactivation function on different catalysts: Ni/CaO–Al_2O_3 (□), Ni/HT70 (○), Ni/HT30 (△) and Ni/HT50 (◆). Reaction conditions: $T = 853$ K, $P_{tot} = 100$ kPa, $P_{CH_4} = 80$ kPa, $P_{H_2} = 5.5$ kPa. Total flow: 50 ml/min.

to the diameter of CNF. It clearly indicates that K is smaller on the smaller CNF, meaning a higher saturation concentration of CNF in Ni bulk. The effect of the diameter of CNF or the Ni crystal size on the equilibrium of precipitation has a much stronger effect for relatively small sizes ($r < 60$ nm), which is also normally the desirable range of CNFs as products.

The model explains well all of the experimental observations in the present work. A small crystal size of Ni will provide a large surface area for the surface reactions, a high diffusion flux area, and a shorter diffusion length, thus leading to a high coking rate. On the other hand, a small crystal size will result in a large saturation concentration of CNF, as shown in Fig. 15, which leads to a low driving force of carbon diffusion (Eq. (12)) and then a lower coking rate. The net effect of the Ni crystal size on the initial rate of CNF growth as shown in Fig. 9 is therefore a result of the compensation of all of the factors. The fact that smaller Ni crystals yield a lower coking rate clearly indicates that the increase in saturation concentration of CNF is dominating. However, it is not possible to simply exclude the changes in Ni surface orientation and the density of steps on differently sized Ni crystals and their effects on CNF growth, although they have not been included in the model.

When the surface area of Ni becomes low enough, the formation of surface carbon from elementary reaction steps can become rate-determining. The model indicates that the lower initial coking rate on Ni/α-Al_2O_3 and Ni/CaO–Al_2O_3 might be a consequence of a lower decomposition rate.

Moreover, the model explains very well the deactivation trends on differently sized Ni crystals. Fig. 16 shows the deactivation function (r/r_0; r and r_0 are the CNF growth rate at time on stream of t and 0, respectively) on differently sized Ni crystals; the smallest crystals appear to have the fastest deactivation rate, and Ni/HT70 and Ni/HT50 appear to exhibit similar deactivation rates. A faster deactivation on smaller sized Ni crystals in Fig. 16 can be explained by a low driving force of diffusion, which results in a higher surface site coverage and consequently enhances the formation of encapsulating carbon via carbon polymerization on the surface (step 11). Ni/CaO–Al_2O_3, with a relatively large crystal size, deactivates slowly. The slow deactivation on large crystals can be explained by the fast diffusion due to low saturation concentration, which leads to a low site coverage of carbon on the Ni surface. However, the faster deactivation on Ni/HT50-74h than Ni/HT50-24h and Ni/HT50-50h seems to be an exception. It might indicate that the effect of Ni crystal size is more complicated in the region near the optimum crystal size, since the small change in crystal size resulted in a very significant change in CNF growth.

The yield of CNF depends on the initial coking rate and on the deactivation rate. In principle, high initial coking rates combined with low deactivation rates will result in high yields of CNF. Unfortunately, our results have indicated that a high coking rate has been accomplished by relatively fast deactivation. A compensation effect of initial coking rate and deactivation leads to an optimum crystal size with respect to the CNF yield. Based on Figs. 9 and 10, it can be concluded that the maximum yield of CNF can be obtained on a Ni crystal size of about 34 nm.

However, it can be argued that supports may have effects other than the Ni crystal size on the coking rates and on the deactivation. The effect of support on the formation of CNFs/CNTs has been widely studied [42–46]. Most of the studies have focused on the effect of support on the diameter and distribution of CNFs as well as on the morphology of CNFs. Vander et al. [46] studied Cu, Fe, and Ni as catalysts and Al_2O_3, CaO, SiO_2, and TiO_2 as support materials. They found that the support influenced not only the diameter of the CNFs but also the density of CNFs as observed in SEM images, which were used as an index of CNF yield. Ni supported on TiO_2 was found to have the highest yield of CNFs. These results were interpreted in terms of an electronic interaction between the metal nanoparticle and the support.

The strong interaction can be attributed to electron donation by the surface. With increasing electron donation to the metal nanoparticles, the strength of interaction between support and metal particles increases. The authors stated that such interaction could dramatically change the crystallography and the electronic state of the metal particles, which can consequently affect the yield, morphology, and structure of CNFs [46]. Interactions between support and Ni particles have also been observed in the present work, which is reflected in the different appearance of the TPR spectra as shown in Fig. 2. However, based on the mechanism presented above, the Ni particles locate on the tip of CNFs after nucleation, and graphene sheets are inserted between Ni particle and the support. This shifts the interaction between the Ni particle and the support on a fresh catalyst into the interaction between the Ni particle and the graphene sheet on the top of the CNFs. Since the surface reactions and other steps involved in the growth of CNFs happen only on/in these Ni particles, the interface between Ni and the support should have very little direct kinetic effect on the steady-state growth of CNFs. The support, of course, is expected to have a strong effect on the initiation of CNFs through the metal-support interaction. Since it is difficult to initiate CNF growth on Ni nanoparticles with a strong interaction with the support, the number of sites for CNF growth can be different on different supports, which will influence the steady-state coking rate. However, we have selected high affinity of carbon formation, namely high pressure of methane, to initiate CNF growth, and minimize the possible effect of nucleation on steady-state kinetics. This explains why we did not observe any induction period during the CNF growth as shown in Fig. 7. From this argument, it follows that the catalyst support affects CNF growth mainly through its crystal size. This has been supported by the fact that Ni/HT50 and Ni/HT70 have similar coking rate and yield of CNF, where the two catalysts have almost identical crystal sizes, but the compositions of the supports are different.

Recently we explored this principle for the synthesis of CNT on supported Fe catalysts in the mixture of CO/H_2 [47]. Different preparation methods have been used to synthesize Fe crystals of different sizes. A maximum growth rate was found on about 10-nm Fe crystals in a mixture of CO/H_2 at 600 °C. A comparison between Fe/SiO_2 and Fe/Al_2O_3 with identical crystal sizes indicates that the support has only a very small effect. The detailed results of the Fe system will be reported elsewhere [47]. These results clearly complement the theory developed in the present work.

The nucleation and growth of CNFs have also been studied by temperature-programmed synthesis. As clearly indicated in Fig. 12, the induction period is longer on the smaller Ni crystals. It has generally been accepted that a supersaturation of carbon in Ni particles is necessary to generate the driving force for diffusion. A higher supersaturation is then required for a smaller crystal, because of its higher saturation concentration of CNFs. In the temperature-programmed synthesis of CNFs, a higher temperature is then needed for initiation of CNFs.

The enhancement of the formation of CNFs in the presence of a small amount of hydrogen has also been observed previously [17,40,48]. However, the effect of hydrogen on the formation of CNF is not straightforward. The presence of hydrogen changes the rates of the surface elementary reaction steps. Higher hydrogen partial pressure can enhance the adsorption of hydrogen and suppress the dissociation of methane. It can also enhance the reverse reaction steps, that is, the gasification of surface carbon. These factors will result in a low surface coverage of carbon. On the other hand, increased site coverage of hydrogen will suppress the polymerization of carbon and thus the formation of encapsulating carbon, resulting in decreased deactivation. At relatively low partial pressures of hydrogen, the suppression of encapsulating carbon is dominating, resulting in an increase in the coking rate with increasing hydrogen partial pressure. Upon a further increase in the hydrogen partial pressure, the suppression of the dissociation of methane or the enhancement of gasification becomes dominating, resulting in a decrease in the coking rate. A maximum coking rate can therefore be achieved at a certain hydrogen partial pressure, which is a function of methane partial pressure, temperature, and crystal size of Ni.

4.3. Size-controlled synthesis of CNFs

The CNFs synthesized on Ni crystals possessing average sizes of 12 and 24 nm have been studied by TEM. The representative TEM images (Figs. 13 and 14) demonstrate the determining role of the catalyst in defining the diameter of CNFs. The CNFs obtained from Ni nanoparticles with average diameters of 12 and 24 nm have diameters of 8 and 25 nm, respectively. A detailed comparison between Ni crystal size distribution and CNF diameter distribution has been presented in Fig. 6. In good agreement with the observation of Cheung et al. [25] for unsupported Fe nanoclusters, a close relationship between the size of the Ni crystal and the diameter of the produced CNFs has also been observed on the supported catalysts. The results clearly show that the size-controlled synthesis of CNFs can be realized by controlling the size of metal particles.

CNF produced on different Ni catalysts during methane decomposition has a very similar nanostructure. In good agreement with previous observations [2], fishbone is the dominating structure of CNF. However, the surface of CNFs on large crystals seems to be smoother, as shown in Figs. 13B and 14B.

Based on the TEM images, the crystallinity of CNFs is rather high, which can be attributed to good crystallinity of the Ni crystals. No other forms of carbon were found by TEM, meaning a high purity of CNFs prepared. This is partially due to the relatively low temperature used in the present work for the synthesis of CNFs, which avoids carbon deposition by gas-phase reactions.

5. Conclusions

Experimental results clearly indicate that the crystal size of Ni has very significant effects on the CNF growth, including the initial coking rate, the deactivation rate, and the final yield of CNF. A model for CNF growth has been proposed that includes surface elementary reaction steps, segregation, and diffusion through the particles and precipitation on the rare side of the Ni particles. The model suggests that the CNF growth has been affected by metal crystal size mainly through the saturation concentration of CNF in Ni bulk, because of changes in the surface tension energy of CNFs with their diameters. A small Ni crystal resulting in a high saturation concentration of CNF in Ni lowers the driving force for the carbon diffusion through the Ni crystals, leading to a fast deactivation and a low final carbon yield. Too great a Ni particle size yields a slow decomposition on the surface due to the low surface area, which reduces the CNF formation. Therefore, an optimal crystal size of Ni of around 34 nm was found for CNF growth, as a result of relatively high initial coking rate and slow deactivation.

For many applications of CNF, smaller diameters are preferred. As illustrated in the present work, such CNFs with small diameters are relatively difficult to synthesize because of their low coking rate and fast deactivation. We believe that many applications, such as catalyst supports, electrode materials, etc., do not need CNFs with extremely small diameters. The results in the present work point out the importance of integrated research for each specific application of CNFs, in which the optimal nanostructure and diameter of CNF should be determined by taking into account both CNF production and application. We also believe that a detailed understanding of the effects of metal crystal size on the initial rate and the deactivation rate of the CNF growth will facilitate the catalyst design for large-scale production of CNFs.

Although the effects of the crystal size on the formation of CNFs were studied only during methane decomposition on Ni catalysts in the present work, the principle can be extended to other reaction systems involving other hydrocarbons and on other catalysts, such as Co, Fe [47], or alloy catalysts. It can also help us to understand many previous results, such as the support effect.

Acknowledgment

The support by the Research Council of Norway is gratefully acknowledged.

References

[1] T.W. Ebbesen, Carbon nanotubes: Preparation and properties, CAPLUS, USA, 1997.
[2] K.P. De Jong, J.W. Geus, Catal. Rev.-Sci. Eng. 42 (2000) 481.
[3] N.M. Rodriguez, M.S. Kim, R.T.K. Baker, J. Phys. Chem. 98 (1994) 13108.
[4] C. Park, E.S. Engel, A. Crowe, T.R. Gilbert, N.M. Rodriguez, Langmuir 16 (2000) 8050.
[5] A. Chambers, C. Park, R.T.K. Baker, N.M. Rodriguez, J. Phys. Chem. B 102 (1998) 4253.
[6] K. Lozano, E.V. Barrera, J. Appl. Polymer Sci. 79 (2000) 125.
[7] H. Dai, J.H. Hafner, A.G. Rinzler, D.T. Colbert, R.E. Smalley, Nature 384 (1996) 147.
[8] H. Dai, J. Kong, C. Zhou, N. Franklin, T. Tombler, S. Fan, in: Handbook of Nanophase and Nanostructured Materials, vol. 4, 2003, p. 96.
[9] A. Oberlin, M. Endo, T. Koyama, J. Crystal Growth 32 (1976) 335.
[10] R.T.K. Baker, M.S. Kim, A. Chambers, C. Park, N.M. Rodriguez, Stud. Surf. Sci. Catal. 111 (1997) 99.
[11] S. Helveg, C. Lopez-cartes, J. Sehested, P.L. Hansen, B.S. Clausen, J.R. Rostrup-Nielsen, F. Abild-Pedersen, J.K. Nørskov, Nature 427 (2004) 426.
[12] R.T.K. Baker, N.M. Rodriguez, Mat. Res. Soc. Symp. Proceed. 349 (1994) 251.
[13] K. Hernadi, A. Fonseca, J.B. Nagy, A. Siska, I. Kiricsi, Appl. Catal. A 199 (2000) 245.
[14] M.A. Ermakova, D.Y. Ermakov, G.G. Kuvshinov, Appl. Catal. A 201 (2000) 61.
[15] J.F. Colomer, C. Stephan, S. Lefrant, G. Van Tendeloo, I. Willems, Z. Konya, A. Fonseca, C. Laurent, J.B. Nagy, Chem. Phys. Lett. 317 (2000) 83.
[16] J.I. Villacampa, C. Royo, E. Romeo, J.A. Montoya, P. Del Angel, A. Monzón, Appl. Catal. A: General 252 (2003) 363.
[17] D. Chen, R. Lodeng, A. Holmen, Stud. Surf. Sci. Catal. 126 (1999) 473.
[18] J.R. Rostrup-Nielsen, Steam Reforming Catalysts: An Investigation of Catalysts for Tubular Steam Reforming of Hydrocarbons, Teknisk Forlag A/S, Copenhagen, 1975.
[19] J.R. Rostrup-Nielsen, NATO Adv. Stu. Inst. Seriers E: Appl. Sci. 54 (1982) 127.
[20] J.R. Rostrup-Nielsen, J. Sehested, Stud. Surf. Sci. Catal. 139 (2001) 1.
[21] M.A. Ermakova, D.Y. Ermakov, G.G. Kuvshinov, L.M. Plyasova, J. Catal. 187 (1999) 77.
[22] J. Hone, B. Batlogg, Z. Benes, M.C. Laguno, N.M. Nemes, A.T. Johnson, J.E. Fischer, Mat. Res. Soc. Symp. Proceed. 633 (2001) A17.1.1.
[23] O. Groning, O.M. Kuttel, C. Emmenegger, P. Groning, L. Schlapbach, J. Vac. Sci. Technol. B: Microelect. Nano. Struc. 18 (2000) 665.
[24] E. Richter, K.R. Subbaswamy, Phys. Rev. Lett. 79 (1997) 2738.
[25] C.L. Cheung, A. Kurtz, H. Park, C.M. Lieber, J. Phys. Chem. B 106 (2002) 2429.
[26] H. Dai, A.G. Rinzler, P. Nikolaev, A. Thess, D.T. Colbert, R.E. Smalley, Chem. Phys. Lett. 260 (1996) 471.
[27] M.A. Ermakova, D.Y. Ermakov, L.M. Plyasova, G.G. Kuvshinov, Catal. Lett. 62 (1999) 93.
[28] R.T.K. Baker, P.S. Harris, R.B. Thomas, R.J. Waite, J. Catal. 30 (1973) 86.
[29] D. Chen, A. Gronvold, H.P. Rebo, K. Moljord, A. Holmen, Appl. Catal. A 137 (1996) L1.
[30] J.W. Snoeck, G.F. Froment, M. Fowles, J. Catal. 169 (1997) 240.
[31] J.W. Snoeck, G.F. Froment, M. Fowles, J. Catal. 169 (1997) 250.
[32] M.V. Twigg, J.T. Richardson, Appl. Catal. A 190 (2000) 61.
[33] J.T. Richardson, M. Lei, B. Turk, K. Forster, M.V. Twigg, Appl. Catal. A 110 (1994) 217.
[34] D. Nazimek, A. Machocki, T. Borowiecki, Ads. Sci. Technol. 16 (1998) 747.
[35] F. Cavani, F. Trifiro, A. Vaccari, Catal. Today 11 (1991) 173.
[36] T. Shishido, M. Sukenobu, H. Morioka, M. Kondo, Y. Wang, K. Takaki, K. Takehira, Appl. Catal. A 223 (2002) 35.
[37] I. Alstrup, J. Catal. 109 (1988) 241.
[38] D. Chen, R. Lodeng, K. Omdahl, A. Anundskas, O. Olsvik, A. Holmen, Stud. Surf. Sci. Catal. 139 (2001) 93.
[39] L.C. Isett, J.M. Blakely, Surf. Sci. 58 (1976) 397.

[40] P.E. Nolan, D.C. Lynch, A.H. Cutler, J. Phys. Chem. B. 102 (1998) 4165.
[41] G.G. Tibbetts, J. Cryst. Grow. 66 (1984) 632.
[42] M.L. Toebes, J.H. Bitter, A.J. van Dillen, K.P. de Jong, Catal. Today 76 (2002) 33.
[43] P.E. Anderson, N.M. Rodriguez, Mat. Res. Soc. Symp. Proceed. 593 (2000) 45.
[44] P.E. Anderson, N.M. Rodriguez, Chem. Mater. 12 (2000) 823.
[45] K. Hernadi, Z. Konya, A. Siska, J. Kiss, A. Oszko, J.B. Nagy, I. Kiricsi, Mater. Chem. Phys. 77 (2003) 536.
[46] R.L. Vander Wal, T.M. Ticich, V.E. Curtis, Carbon 39 (2001) 2277.
[47] Z. Yu, D. Chen, B. Tøtdal, A. Holmen, Accepted for publication in Catal. Today.
[48] P.E. Nolan, M.J. Schabel, D.C. Lynch, Carbon 33 (1995) 79.